Chapter 4.

Molecular dynamics on a curved substrate

The mathematical concept of space-time curvature has fundamentally changed the way we perceive and describe the physical world from the cosmological to the microscopic scale. In soft matter physics, substrate curvature has been shown to have a remarkable effect on two-dimensional films confined on it [5, 90, 104, 115, 124]. A common numerical method used to model such soft matter systems is molecular dynamics. Performing molecular dynamics on curved surfaces is not a straightforward task. The equations of motion become increasingly harder as the curvature becomes more complex. Where in the absence of curvature a free particle follows a straight line, in the presence of curvature a free particle follows a generalization of a straight line called a *geodesic* [113], see appendix D. Already in flat space, conventional numerical solutions to the equations of motion, called *integrators*, often fail to preserve the conserved quantities of these equations of motion, such as energy and momentum [103, 129, 136]. Examples of such integrators are *Forward Euler* and *Runge–Kutta method*, see appendices I and J, respectively. When an integrator *does* preserve these symmetries it is called *symplectic*. Examples of symplectic integrators in the absence of curvature are *Symplectic Euler* and *Velocity Verlet*, see appendices K and L. Even when a certain integrator is symplectic in the absence of curvature, however, it is not necessarily so in the presence of curvature, as these integrators are not explicitly designed to cope with curvature.

In this chapter, we will use the method of variational integrators [103, 129, 136] to derive a novel symplectic integrator that solves Newton's equations in the presence of curvature. First, we will derive Newton's equations in the presence of curvature. Second, we discuss how to discretize the equations of

motions in time whilst preserving the conserved quantities — by respecting the Lagrangian symmetries in accordance to Noether's theorem. Third, we apply the discussed techniques to derive a novel symplectic integrator algorithm that solves Newton's equations in the presence of curvature. Finally, we will illustrate how to apply the integrator to study the two-dimensional melting transition in the presence of curvature and give some preliminary results.

4.1 Newton's equations in the presence of curvature

Newton's equations on a Riemannian manifold can be found using Lagrangian mechanics, see appendix C. Let us define the metric tensor on our manifold to be $g_{\mu\nu}$ and we find the Lagrangian:

$$L = \tfrac{1}{2} m g_{\mu\nu} \dot{x}^\mu \dot{x}^\nu - V(x^\rho), \tag{4.1}$$

where m is the mass and $V(x^\rho)$ is some arbitrary interaction potential. Upon applying the Euler–Lagrange equations — eq. (C.3) — we find the conservative version of Newton's equations of motion in the presence of curvature:

$$m\left(\ddot{x}^\mu + \Gamma^\mu_{\sigma\rho} \dot{x}^\sigma \dot{x}^\rho\right) = -g^{\mu\nu} \partial_\nu V, \tag{4.2}$$

which can be made non-conservative by realizing that the right-hand side of eq. (4.2) is a force:

$$F^\mu = m\left(\ddot{x}^\mu + \Gamma^\mu_{\sigma\rho} \dot{x}^\sigma \dot{x}^\rho\right). \tag{4.3}$$

The symbols $\Gamma^\mu_{\sigma\rho}$ in eqs. (4.2) and (4.3) are called the Christoffel symbols of the second kind. Christoffel symbols of the second kind can be defined in terms of the metric tensor as:

$$\Gamma^\mu_{\sigma\rho} = \tfrac{1}{2} g^{\mu\lambda} \left(\partial_\sigma g_{\lambda\rho} + \partial_\rho g_{\sigma\lambda} - \partial_\lambda g^{\sigma\rho}\right), \tag{4.4}$$

Christoffel symbols of the first kind $\Gamma_{\mu\sigma\rho}$ are defined as such:

$$\Gamma_{\mu\sigma\rho} = g_{\mu\lambda}\Gamma^\lambda_{\sigma\rho} = \tfrac{1}{2}\left(\partial_\sigma g_{\mu\rho} + \partial_\rho g_{\sigma\mu} - \partial_\mu g_{\sigma\rho}\right). \tag{4.5}$$

It is worth noting that the Christoffel symbols are *not* tensors — they change when the coordinate system changes. From eq. (4.3) we obtain the geodesic equations

$$\ddot{x}^\mu + \Gamma^\mu_{\sigma\rho} \dot{x}^\sigma \dot{x}^\rho = 0. \tag{4.6}$$

The geodesic equations generalize the notion of a straight path♠ in the presence of curvature — see appendix D for a more detailed derivation.

♠Often, a straight path is also the shortest.

4.2 Variational integrators

Among the common methods to solve second order dynamical systems[♠] numerically are the Forward Euler and Runge–Kutta methods, see appendices I and J. For Newtonian systems there are, however, some shortcomings associated with these methods. The problem becomes apparent when considering the total energy or Hamiltonian H of such a system. When we look at $H_{i+j} - H_i > 0$ for $j > 0$ we realize that with increasing time steps the total energy of the system rises, see appendix M. The algorithms fail to preserve the Hamiltonian which ought to be constant, see appendix B. As a consequence, these numerical solutions will hence deviate from the actual path in phase space. The path could even be attracted by different fixed points — or worse, diverge, causing numerical *explosions*. The fundamental problem is that these algorithms do not respect the Lagrangian symmetries giving rise to conserved quantities by Noether's theorem. An energy-conserving numerical method would be highly desirable. Such an integrator would be symplectic.[♡] Symplectic integrators can be found using the method of *variational integrators* [103, 129, 136].

The idea behind variational integration is best illustrated within Lagrangian mechanics. We know how to derive Newton's equations of motion, eqs. (4.2) and (B.4), from the Lagrangian L using the Euler–Lagrange equation, eq. (C.3), by the so-called stationary action principle, as discussed in section 4.1 and appendix C. The Lagrangian L possesses symmetries that generate conserved quantities. Here, we want to solve the equations of motion for discrete time steps, recurrently, as our aim is to let a computer solve them. Hence, if we formulate a discretized version of the stationary action principle — appropriately — it should yield a discrete solution of the equations of motion *with* conservation of Lagrangian symmetries — at least up to certain order. The resulting numerical scheme is, hence, symplectic by definition. This is essentially what the method of variational integration accomplishes. We will continue to describe how the action can be discretized.

[♠] Systems of differential equations.

[♡] Strictly, symplecticity only preserves volume in phase space and total energy is only conserved for exponentially long periods of time. For variational integrators, however, also kinetic energy — or momentum — is strictly conserved.

Let us define the timestep h such that $t_{i+1} = t_i + h$. A discretized Lagrangian $L_D(x^\mu, \dot{x}^\mu)$ is found by:

$$L_D(x_i^\mu, x_{i+1}^\mu) = \int_{t_i}^{t_{i+1}} L(x^\mu, \dot{x}^\mu, t)\,\mathrm{d}t. \tag{4.7}$$

The action, eq. (C.1), in terms of the discretized Lagrangian is then given by

$$S = \sum_i L_D(x_i^\mu, x_{i+1}^\mu). \tag{4.8}$$

Now let us introduce the discrete-time partial derivative $\partial_\sigma^i = \frac{\partial}{\partial x_i^\sigma}$ for which:

$$\partial_\sigma^i x_k^\mu = \delta_\sigma^\mu \delta_{ik}. \tag{4.9}$$

The Euler–Lagrange equations are the equations that find the stationary points in the action, analogous to eqs. (C.2) and (C.3) in appendix C. The time-discrete version is given by:

$$\partial_\sigma^i S = 0, \tag{4.10}$$

which, hence, yields the discrete Euler–Lagrange equations:

$$\partial_\sigma^i L_D(x_{i-1}^\mu, x_i^\mu) + \partial_\sigma^i L_D(x_i^\mu, x_{i+1}^\mu) = 0. \tag{4.11}$$

The discrete Euler–Lagrange equations then yield the discrete-time equations of motion, *whilst preserving the Lagrangian symmetries*. Note that the discrete Lagrangian $L_D(x_i^\mu, x_{i+1}^\mu)$ is solely a function of position x_i^μ and not of velocity $\dot{x}_i^\mu$. The new velocity can be found explicitly by the following formula:

$$\dot{x}_{i+1}^\mu = \tfrac{1}{m}\delta^{\mu\sigma}\partial_\sigma^{i+1} L_D(x_i^\mu, x_{i+1}^\mu). \tag{4.12}$$

The old velocity is given by:

$$\dot{x}_i^\mu = -\tfrac{1}{m}\delta^{\mu\sigma}\partial_\sigma^{i} L_D(x_i^\mu, x_{i+1}^\mu). \tag{4.13}$$

This formula is generally implicit. Fortunately this is not a problem as most integration schemes only rely on eq. (4.12).

The method of variational integrators can be used to derive the symplectic Euler method and higher-order Velocity verlet method, reviewed in appendices K and L.

4.3 Symplectic integration with curvature

We will now move on to derive the analog of the symplectic Euler scheme in the presence of Riemannian curvature.[♠] The derivation will thus be very similar to the symplectic Euler derivation discussed in appendix K which also uses the variational integration method described in section 4.2. Now, however, we will use a Lagrangian that incorporates curvature $L = \frac{1}{2} m g_{\mu\nu} \dot{x}^\mu \dot{x}^\nu - V(x^\rho)$, as discussed in section 4.1 — particularly eq. (4.1). We will continue to discretize this Lagrangian using eq. (4.7). We approximate the integral using the rectangle method — see eq. (H.6) in appendix H. We will additionally invoke a discrete velocity:

$$\dot{x}^\mu = \tfrac{1}{h} \left(x^\mu_{i+1} - x^\mu_i \right). \tag{4.14}$$

Doing so results into the following discrete Lagrangian:

$$L_D^{\text{rect}}(x^\mu_i, x^\mu_{i+1}) = \tfrac{m}{2h} \left(g^i_{\mu\nu} x^\mu_{i+1} x^\nu_{i+1} - 2 g^i_{\mu\nu} x^\mu_{i+1} x^\nu_i + g^i_{\mu\nu} x^\mu_i x^\nu_i \right) - h V_i. \tag{4.15}$$

Note that contrary to the Euclidean space case, the metric $g_{\mu\nu}(x^\mu)$ in the Lagrangian *is* a function of position. Hence, its discrete counterpart is a function of the discrete position $g^i_{\mu\nu} = g_{\mu\nu}(x^\mu_i)$.[♡] We will then continue to apply the discrete Euler–Lagrange equations, eq. (4.11), to our discrete Lagrangian, eq. (4.15). In order to do so, we establish the following identities:

$$\partial^i_\sigma g^j_{\mu\nu} x^\mu_k x^\nu_l = \delta_{ij} \left(\Gamma^j_{\nu\sigma\mu} + \Gamma^j_{\mu\sigma\nu} \right) x^\mu_k x^\nu_l + g^j_{\mu\nu} \left(\delta_{ik} \delta^\mu_\sigma x^\nu_l + \delta_{il} x^\mu_k \delta^\nu_\sigma \right), \tag{4.16}$$

which holds because[♣]

$$\partial^i_\sigma g^j_{\mu\nu} = \delta_{ij} \left(\Gamma^{\lambda\, j}_{\sigma\mu} g^j_{\lambda\nu} + \Gamma^{\lambda\, j}_{\sigma\nu} g^j_{\mu\lambda} \right) = \delta_{ij} \left(\Gamma^j_{\nu\sigma\mu} + \Gamma^j_{\mu\sigma\nu} \right). \tag{4.17}$$

Using these identities we apply the Euler–Lagrange equations and obtain:

$$\begin{aligned} &\Gamma^i_{\nu\sigma\mu} \left(x^\mu_{i+1} x^\nu_{i+1} + x^\mu_i x^\nu_i \right) - \left(\Gamma^i_{\nu\sigma\mu} + \Gamma^i_{\mu\sigma\nu} \right) x^\mu_{i+1} x^\nu_i + \\ &g^i_{\sigma\mu} \left(x^\mu_i - x^\mu_{i+1} \right) + g^{i-1}_{\sigma\mu} \left(x^\mu_i - x^\mu_{i-1} \right) - \tfrac{h^2}{m} \partial^i_\sigma V_i = 0, \end{aligned} \tag{4.18}$$

[♠] As far as is known to the author, this will be the first explicit publication of this kind of symplectic integrator for Riemannian manifolds.

[♡] In the absence of curvature this remark becomes irrelevant because then $g_{\mu\nu} = \delta_{\mu\nu}$ an therefore $\delta^i_{\mu\nu} = \delta^j_{\mu\nu}$ for all i, j — see eq. (K.2) in appendix K.

[♣] The Christoffel symbols of first and second kind $\Gamma_{\mu\sigma\rho}$ and $\Gamma^\mu_{\sigma\rho}$ are respectively defined in eqs. (4.4) and (4.5).

which can be simplified by introducing the variable $\epsilon_i^\mu = x_{i+1}^\mu - x_i^\mu$ yielding:

$$\Gamma^i_{\nu\sigma\mu}\epsilon_i^\mu\epsilon_i^\nu - g^i_{\sigma\mu}\epsilon_i^\mu + g^{i-1}_{\sigma\mu}\left(x_i^\mu - x_{i-1}^\mu\right) - \tfrac{h^2}{m}\partial^i_\sigma V_i = 0. \tag{4.19}$$

Now let us introduce the following variables for our convenience:

$$A^i_{\sigma\mu\nu} = \Gamma^i_{\nu\sigma\mu}, \tag{4.20}$$

$$B^i_{\sigma\mu} = -g^i_{\sigma\mu}, \tag{4.21}$$

$$C^{i,i-1}_\sigma = g^{i-1}_{\sigma\mu}\left(x_i^\mu - x_{i-1}^\mu\right) - \tfrac{h^2}{m}\partial^i_\sigma V_i. \tag{4.22}$$

We then solve for ϵ_i^μ in the equation:

$$A^i_{\sigma\mu\nu}\epsilon_i^\mu\epsilon_i^\nu + B^i_{\sigma\mu}\epsilon_i^\mu + C^{i,i-1}_\sigma = 0. \tag{4.23}$$

Since denoting a particular timestep i at this point, has become unnecessary we may drop the Latin time index in order simplify even further:

$$A_{\sigma\mu\nu}\epsilon^\mu\epsilon^\nu + B_{\sigma\mu}\epsilon^\mu + C_\sigma = 0. \tag{4.24}$$

A natural way to solve eq. (4.24) numerically would be to apply fixed-point iterations as discussed in appendix F, eq. (F.12). Since, $B_{\sigma\mu} = -g_{\sigma\nu}$ is just minus the metric and hence $B_{\sigma\mu}$ is by definition invertible, we may proceed using the fixed-point iteration scheme. The fixed-point function is given by

$$F^\mu(\epsilon^\mu) = g^{\mu\sigma}A_{\sigma\rho\nu}\epsilon^\rho\epsilon^\nu + g^{\mu\sigma}C_\sigma. \tag{4.25}$$

Now let us assume that the ϵ^μ is small as it scales with the small timestep h. The fixed-point equations, eq. (4.25), then have a known solution up to first order in h:

$$F^\mu(\epsilon^\mu) = g^{\mu\sigma}C_\sigma + \mathcal{O}(h^2), \tag{4.26}$$

hence we can define ϵ_0^μ, the initial value for the fixed-point iteration:

$$\epsilon_0^\mu = g^{\mu\sigma}C_\sigma + \mathcal{O}(h^2), \tag{4.27}$$

which approximately solves eq. (4.25). As the fixed-point iteration algorithm converges we find the end result $\bar{\epsilon}^\mu$. Using eq. (4.12) we find that the new position and velocity on the manifold are given by

$$x^\mu_{i+1} = x^\mu_i + \bar{\epsilon}^\mu_i, \tag{4.28}$$

$$\dot{x}^\mu_{i+1} = \tfrac{1}{h}\bar{\epsilon}^\mu_i. \tag{4.29}$$

When $g^{\mu\nu} \to \delta^{\mu\nu}$ and therefore $\Gamma_{\mu\sigma\nu} \to 0$, we recover the symplectic Euler scheme as described in appendix K. In addition, we may modify our method a bit to solve the equations of motion for non-conservative systems. This can be done by substituting $-\partial_\sigma V_i$ by an arbitrary force F_i^μ in C_σ yielding:

$$C_\sigma^{i,i-1} = g_{\sigma\mu}^{i-1}\left(x_i^\mu - x_{i-1}^\mu\right) + \tfrac{h^2}{m}\delta_{\sigma\mu}F_i^\mu. \tag{4.30}$$

Using eq. (4.30) instead of eq. (4.22) in the fixed-point iteration scheme, eqs. (4.25) and (4.27) will produce discretized equations of motion in the presence of curvature for non-conservative systems.

4.4 Melting on curved substrates

The nature of two-dimensional crystal melting has been a controversial topic in the last decades [159]. According to Kosterlitz, Thouless, Halperin, Nelson and Young (KTHNY), a melting two-dimensional crystal first loses translational order and then orientational order at distinct temperatures. This occurs due to the emergence of topological defects in the crystal. Alternative scenarios have proposed a discontinuous melting transition mediated by the nucleation of grain boundaries. Although there is no definite consensus on the matter on *all* types of crystals, KTHNY melting transitions have been observed experimentally in colloidal systems [80, 160].

4.4.1 Topological defects in crystals

In a two-dimensional crystal there may be two types of topological defects. First, there are disclinations. Disclinations are crystal sites with an irregular coordination number, the number of bonds. An under- or over-coordinated site is irregular and breaks orientational order. These irregularities are called disclinations. For example, in a triangular lattice the regular coordination number is six — as depicted by the black sites in fig. 4.1. A disclination comes with a topological charge. The topological charge of a disclination is found by winding around it. In the example this reveals that a fivefold (blue) and a sevenfold (red) disclination have a topological charge of $j_5 = -\frac{\pi}{3}$ and $j_7 = \frac{\pi}{3}$, respectively. Secondly, there are dislocations. A dislocation is a dipole of disclinations that breaks translational order. Upon winding around a dislocation we find that it is a defect of vectorial order having both a size — the separation and charge of the dipole pair — and an orientation — the relative orientation of the dipole pair. A vector that describes a dislocation is

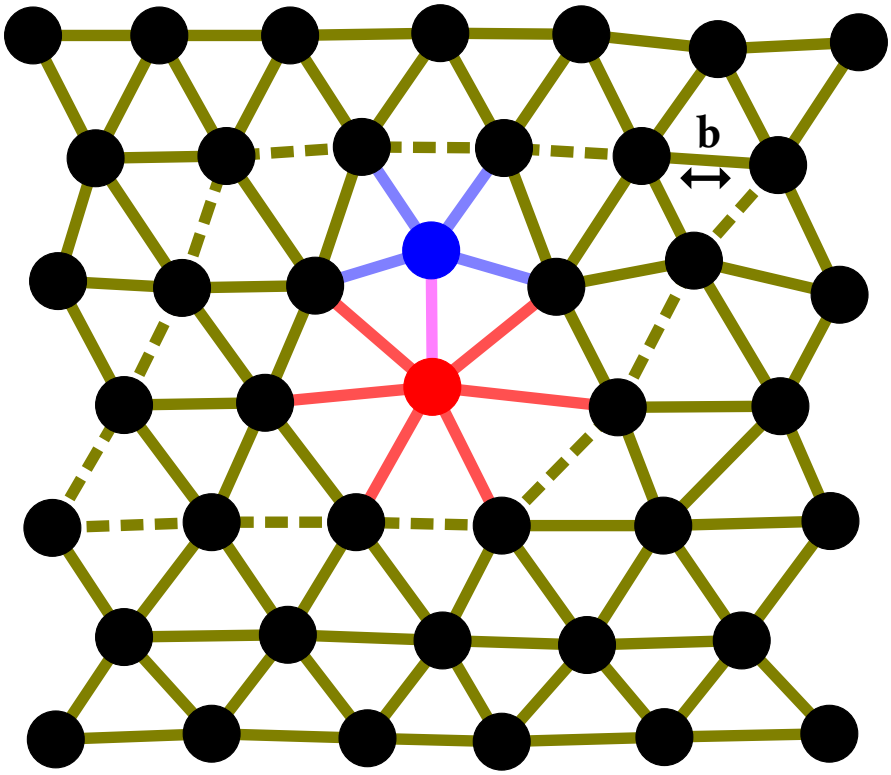

Figure 4.1: A triangular lattice with two disclinations of opposite charge tightly bound to form a dislocation. The blue point is fivefold coordinated forming a negatively charged defect. The red point is sevenfold coordinated forming a positively charge defect. The pink bond binds the two disclinations forming a dislocation. The dashed lines (olive) wind a path of three hops in every direction around the dislocation. As this path cannot close in on itself without taking *one* extra step we conclude that this defect breaks translational order as characterized by the Burgers vector $\boldsymbol{b}$. The sign of the Burgers vector is set by convention.

the Burgers vector $\boldsymbol{b}$, which is found by winding around the dislocation and finding a vector perpendicular to the dipolar separation vector. On a triangular lattice a unit sized Burgers vector $|\boldsymbol{b}| = 1$ can only have six orientations along the principal axes of the crystal. Note how a dipole of dislocations — an irregularity with two dislocations with opposite Burgers vectors right next to each other — is a neutral object as winding around such an irregularity yields no topological charge whatsoever.

4.4.2 KTHNY theory

A perfect triangular lattice at zero temperature has no defects at all. In accordance with KTHNY theory, upon increasing the temperature of such a crystal tight dipoles of dislocations emerge. Increasing the temperature even more, these dipoles of dislocations begin to unbind, breaking translational order. At this stage only translational order is broken. Orientational order, however, remains and the systems resides in the so-called *hexatic* phase. At even higher temperatures, individual dislocations unbind into two disclinations of opposite charge, breaking the residual orientational order and yielding the liquid phase. We see that the entire crystal to liquid melting transition is mediated by the emergence of topological defects.

4.4.3 Defects and curvature

Temperature is not the only reason topological defects may emerge. Stresses and strains in the system may also produce topological defects, in an attempt to screen these strains and stresses with topological charges. Likewise, in the presence of curvature, which invokes stresses and strains, topological charges arise as a screening mechanism. Positively charged disclinations are attracted to regions of positive Gaussian curvature. Similarly negatively charged disclinations are attracted to regions of negative Gaussian curvature. Dislocations reside somewhere in-between the regions of positive and negative Gaussian curvature as they can be viewed as disclination dipoles.

Analytically, the free energy of a crystal with defects in the presence of curvature according to elasticity theory is given by: [104]

$$F = \tfrac{Y}{2} \int \mathrm{d}A \int \mathrm{d}\tilde{A} \left(S(\boldsymbol{x}) - K(\boldsymbol{x})\right) \frac{1}{\Delta^2_{\boldsymbol{x}\tilde{x}}} \left(S(\tilde{\boldsymbol{x}}) - K(\tilde{\boldsymbol{x}})\right), \tag{4.31}$$

where Y is the Young modulus, S is the distribution of unbound topological defects, K is Gaussian curvature and Δ^2 the biharmonic operator. The free energy in terms of the Airy stress function χ is given by:

$$F = \tfrac{1}{2Y} \int \mathrm{d}A (\Delta\chi(\boldsymbol{x}))^2. \tag{4.32}$$

Combining eqs. (4.31) and (4.32) we find the following differential equation:

$$\Delta^2\chi(\boldsymbol{x}) = Y\left(S(\boldsymbol{x}) - K(\boldsymbol{x})\right). \tag{4.33}$$

In the absence of defects the latter becomes

$$\Delta^2\chi(\boldsymbol{x}) = -YK(\boldsymbol{x}), \tag{4.34}$$

yielding an equation that describes the Airy stress function in terms of curvature only. From the Airy stress function we may obtain the geometric potential for dislocations D given by: [104]

$$D(\boldsymbol{x}, \boldsymbol{b}_i) = \boldsymbol{b}_i \epsilon_{ij} \nabla_j \chi(\boldsymbol{x}). \tag{4.35}$$

At zero temperature, dislocations will distribute in regions where they minimize the elastic energy in accordance to the dislocation potential in eq. (4.35).

4.4.4 Dislocation dynamics

As a dislocation terminates a row of sites in a crystal, it is energetically more favorable to nucleate dislocations in tight pairs. Dislocations can easily move around parallel to the Burgers vector orientation. This motion is called *glide*. When a dislocation moves in any other direction that is not parallel to the Burgers vector the motion is called *climb* and generally costs much more energy due to the required diffusive mechanisms. The dislocation pair hence separates by having both of its dislocations glide away from each other. Nucleating a dislocation, and therefore also a dislocation pair, costs energy. The energy per nucleated dislocation is called the core energy E_c.

Dislocations interact with other dislocations. The pairwise dislocation–dislocation potential takes the following form:

$$V_{\mathrm{dd}}(\boldsymbol{b}_i, \boldsymbol{b}_j) = \tfrac{Y}{4\pi} \left(\boldsymbol{b}_i \boldsymbol{b}_j \log\left(\frac{\boldsymbol{r}_{ij}}{a}\right) + \frac{(\boldsymbol{b}_i \boldsymbol{r}_{ij})(\boldsymbol{b}_j \boldsymbol{r}_{ij})}{\boldsymbol{r}_{ij}^2} \right), \tag{4.36}$$

where $\boldsymbol{r}_{ij}$ is the distance between the two dislocations with Burgers vectors $\boldsymbol{b}_i$ and $\boldsymbol{b}_j$ and a is the lattice spacing of the crystal [42]. Additionally, two dislocations of opposite orientation may glide back into each other and annihilate — this is the opposite process of dislocation nucleation. Likewise, two dislocations with different but not equal or opposite orientations may glide into each other and annihilate, resulting in one new dislocation with an intermediate orientation, but equal topological charge. Conversely the reverse process may also occur. For instance on the triangular lattice, the dislocation b_θ and $b_{\theta+\frac{2\pi}{3}}$ may add up to one single dislocation $b_{\theta+\frac{\pi}{3}}$.

In the presence of curvature, dislocation pairs may nucleate in regions where the nucleation energy is sufficiently small. In general, the regions of preferred dislocation pair nucleation are not solely determined by the geometric potential in eq. (4.35). Dynamic constraints play a role as well. The system can only minimize energy through a series of moves consisting of coordinated glide, nucleation and annihilation reactions. As some operations seem entropically hard to reverse, the system may become arrested in some local minimum. In addition, the geometric potential may make dislocation glide energetically costly, as it leaves a local minimum.

4.4.5 Melting on curved substrates

An effective Hamiltonian for dislocations in a curved crystal is:

$$H_{\text{disl}}(\boldsymbol{x}) = NE_c + \sum_i^N D(\boldsymbol{x}, \boldsymbol{b}_i) + \sum_{i>j}^N V_{\text{dd}}(\boldsymbol{b}_i, \boldsymbol{b}_j), \tag{4.37}$$

where N is the number of dislocations in the system. When generating equilibrium states from this Hamiltonian however, one should consider that some states may not be accessed due to dislocation dynamics. For instance, the lowest energy configuration of a curved crystal with one dislocation is found when the dislocation resides in the minimum of the dislocation potential eq. (4.35). This state might never occur, however, if dislocation pairs are nucleated in on the wrong row, as dislocations are only allowed to glide. At this point, it is obvious to expect dislocations and also disclinations to have spatial preferences, depending on the curvature. Therefore, a crystal in the presence of curvature may melt inhomogeneously allowing crystal, hexatic and liquid phases to simultaneously exist at different locations of the sample.

It is, however, hard to establish if the dislocation density $\sigma_{\text{disl}}(\boldsymbol{x})$ is purely dominated by energetics and thus follows from

$$\sigma_{\text{disl}}(\boldsymbol{x}) \propto e^{-\beta H_{\text{disl}}(\boldsymbol{x})}, \tag{4.38}$$

or whether it is determined primarily by dislocation-dynamic effects.

4.4.6 Computational studies of melting and curvature

Monte Carlo simulations have studied the distribution of dislocations in the presence of curvature at zero temperature [99]. Although the Monte Carlo method should also work at finite temperature, curved space melting was never thoroughly investigated because the algorithm gets slower as temperatures increase. An alternative candidate method would be molecular dynamics.[♠] Molecular dynamics is a numerical method that solves Newton's equations of motion for many interacting particles — the so-called generalized N-body problem. Here we will solve Newton's equations of motion for many interacting particles in the presence of curvature. The integration scheme to solve Newton's equations in the presence of curvature — which is the main subject of this chapter — is discussed in section 4.3. Apart from the integration method; the choice of curvature, boundary and initial conditions and ensemble preparations are important. We choose the surface to be of a form represented by the two-dimensional Monge patch, see appendix E. A Monge patch, defines a curved surface by introducing a scalar function $f : \mathbb{R}^2 \to \mathbb{R}$ called the Monge function which is embedded in a three-dimensional space $\mathbb{R}^3$. We will simulate for the following Monge functions:

$$f_{\text{bump}}(x, y) = Ae^{-K\left(x^2+y^2\right)}, \tag{4.39}$$

$$f_{\text{egg}}(x, y) = A\cos(K_x x)\cos(K_y y), \tag{4.40}$$

which we will refer to as the Gaussian bump eq. (4.39) and egg carton eq. (4.40), respectively. Here, for both Monge functions, A is the amplitude. K is the width of the Gaussian bump and $\{K_x, K_y\}$ set the periodicities of the egg carton surface. We will choose an $L_x \times L_y$ with $L_x \approx L_y$ nearly square simulation box with the origin in the middle and with periodic boundary conditions. In order to ensure periodicity in the Monge functions, we apply the constraints $K^{-1} \ll L^2$ and $K_x = \frac{2\pi}{L}n$ and $K_y = \frac{2\pi}{L}m$ with $n, m \in \mathbb{N}$. We initialize $N \in \mathbb{N}$ particles in a triangular lattice with lattice spacing a.[♡]

[♠] Molecular dynamics is introduced in appendix O.

[♡] For a possible algorithm to generate a triangular lattice see appendix section Q.2.

N	q_x	q_y
780	26	15
5822	71	41
10864	97	56
17466	123	71
32592	168	97
43456	194	112
65964	239	138
81090	265	153
97776	291	168
130368	336	194
151316	362	209
173824	388	224
216500	433	250
243270	459	265
271600	485	280

N	q_x	q_y
293328	504	291
324360	530	306
356952	556	321
417094	601	347
453948	627	362
492362	653	377
562588	698	403
605264	724	418
649500	750	433
729810	795	459
778308	821	474
828366	847	489
866000	866	500
918760	892	515
973080	918	530

Table 4.1: An incomplete list of special numbers up to a million that generate a triangular lattice in an approximate square. N is the number of particles, q_x and q_y are the number of unit cells in the x and y direction respectively. The tolerance on q_x and q_y is at most 0.01.

We are trying to prepare a triangular lattice with N particles inside a square box with periodic boundary conditions. In order to tile the square box with $q_x \times q_y$ tiles we require[♠]

$$N = 2q_x q_y = \frac{2L^2}{\sqrt{3}\,a}. \tag{4.41}$$

As eq. (4.41) has to be satisfied we have to find the special numbers that approximately fit; some of these numbers are listed in table 4.1. The procedure is depicted in fig. 4.2. The velocity of the particles is randomly assigned according to the generalized equipartition theorem, respecting the curvature. This can be done as follows. The equipartition theorem states:

$$\langle x^\mu \partial_\nu H_{\text{kin}} \rangle = \delta^\mu_\nu k_B T. \tag{4.42}$$

[♠] Tiles stack in integer values, hence: $q_x, q_y \in \mathbb{N}$.

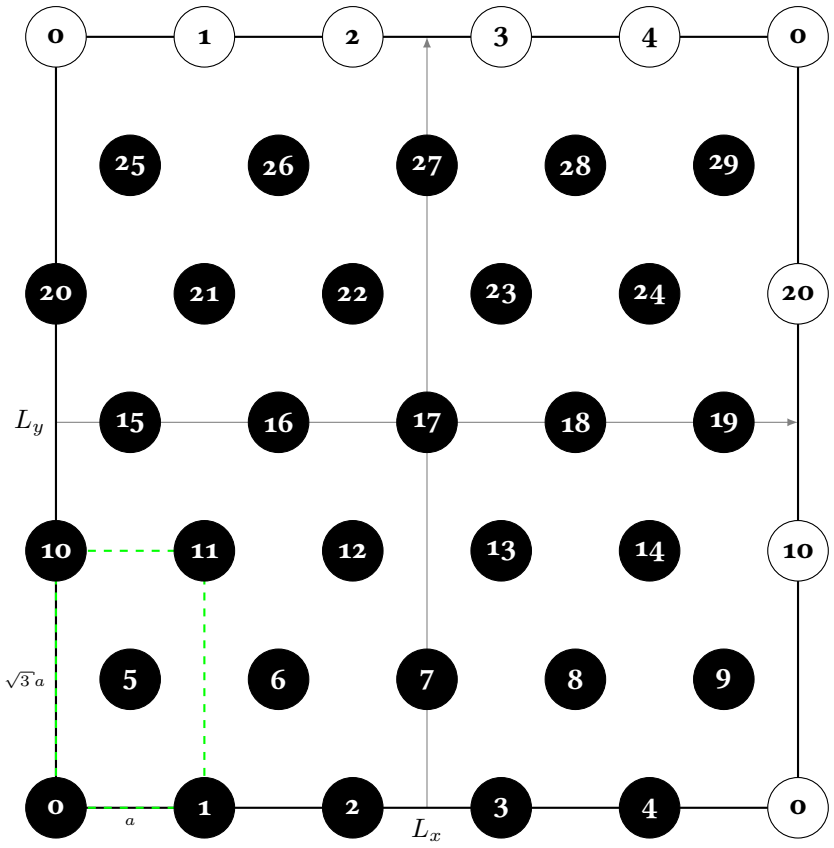

Figure 4.2: Depiction of $N = 30$ black particles in a triangular lattice within the simulation box of $L_x \times L_y$ ($q_x = 5$ and $q_y = 3$). Particle seventeen lies in the origin of the chosen coordinate system. The white particles are image particles present because of periodic boundary conditions. The black lines are the boundaries of the system. The gray lines are the base-axes. The green dashed lines depict the unit cell containing two particles, in this case, once particle five and a quarter times particles zero, two, ten and eleven.

In this case, the kinetic part of the Hamiltonian is given by:

$$H_{\text{kin}} = \tfrac{1}{2} m g_{\mu\nu} \dot{x}^\mu \dot{x}^\nu. \tag{4.43}$$

By using eqs. (4.42) and (4.43) the following equality is found:

$$\langle g_{\mu\nu} \dot{x}^\mu \dot{x}^\nu \rangle = g_{xx} \langle \dot{x}^2 \rangle + g_{yy} \langle \dot{y}^2 \rangle + 2 g_{xy} \langle \dot{x}\dot{y} \rangle = \tfrac{2 k_B T}{m} \tag{4.44}$$

If the problem is diagonalized in the eigenbasis of the metric $g_{\mu\nu}$ this equation simplifies to:

$$\langle \dot{a}^2 \rangle + g \langle \dot{b}^2 \rangle = \tfrac{2 k_B T}{m} \tag{4.45}$$

Where $\dot{a}$ and $\dot{b}$ are eigencoordinates of $g_{\mu\nu}$. Using Maxwell–Boltzmann statistics the variances of the velocity in the $\dot{a}$ and $\dot{b}$ direction are given by:

$$\mathrm{e}^{-\frac{H_{\text{kin}}}{k_B T}} = \mathrm{e}^{-\frac{m(\dot{a}^2 + g\dot{b}^2)}{2 k_B T}} = \mathrm{e}^{-\frac{\dot{a}^2}{2\sigma_{\dot{a}}^2}} \mathrm{e}^{-\frac{\dot{b}^2}{2\sigma_{\dot{b}}^2}}, \tag{4.46}$$

and therefore:

$$\sigma_{\dot{a}}^2 = \tfrac{k_B T}{m}, \qquad \sigma_{\dot{b}}^2 = \tfrac{k_B T}{g m}. \tag{4.47}$$

From the variances and initial particle positions,[♠] random initial velocities corresponding with a certain (fixed) temperature can be found by generating two random numbers from a normal distribution[♡] and multiplying them with their desired variances. The mean of the velocity distribution is zero, since the system is desired to be without flow. Finally, the random numbers need to be transformed back from the eigenbasis of $g_{\mu\nu}$ to the original basis, which is done by a simple base transformation.

Note that the initial conditions chosen for the simulations are not ideal, since the simulation is not started in the ground state of the system, because a flat space triangular lattice is *not* the ground state in curved space. Unfortunately, finding the real curved space ground state is a very hard generalized Thomson-like problem which currently remains unsolved [124, 173]. Therefore the lower limit of the energy in the system is not only controlled by the temperature, but also by the curvature. One way to resolve this issue by minimizing geometric frustration is called quenching: the idea is to run a

[♠] The metric determinant $g = g(x^\rho)$ is position-dependent.

[♡] A uniform random generator can be transformed into a normally distributed random generator by using, for instance, a Box–Muller transformation.

molecular dynamics simulation while occasionally resetting the kinetic energy to zero. The most effective timing to set the kinetic energy to zero is when the kinetic energy is at its maximum and the potential energy is therefore minimal, assuming constant total energy, because the potential energy must be minimized to obtain a local ground state.

The described scheme will simulate particles in the microcanonical ensemble. To obtain a canonical ensemble a linear damping term and a Langevin random force term are introduced — this is the so-called Langevin thermostat.

4.4.7 Preliminary results

Using the procedure as described in section 4.4.6 we prepare our molecular dynamics simulations in the microcanonical ensemble. Let us first analyze the results of such simulations on a Gaussian bump surface, see eq. (4.39). Upon performing one simulation for $N = 17466$ particles in a box with the approximate dimensions $L \times L$ for a small finite temperature — after relaxation[♠] — we typically find a simulation snapshot as depicted fig. 4.3. We observe that the individual dislocations are oriented with their Burgers vectors perpendicular to the radial direction with respect to the top of the bump; fivefold disclinations (blue) facing towards the top and sevenfold disclinations (red) facing away from the bump. The dislocation distribution at low density for a Gaussian bump is found using eq. (4.38) neglecting dislocation–dislocation interactions given by eq. (4.36) in the effective Hamiltonian eq. (4.37). We obtain

$$\sigma_6(x^\rho) \propto \mathrm{e}^{-\beta \min_{\theta\in[0,2\pi]} D(x^\rho, \mathbf{b}(\theta))}, \tag{4.48}$$

where θ is the orientation of the Burgers vector. Hence, we find that $\mathbf{b}(\theta)$ is always perpendicular to the radial direction. The theoretical dislocation density for a Gaussian bump found by using eq. (4.48) is plotted in fig. 4.4.[♡] Upon doing numerous simulations with different random instances of the same initial conditions we can generate a dislocation density profile for the simulations and compare it to this simple estimate. This is done in fig. 4.5,

[♠] Meaning the initial condition is first quenched to zero temperature after which the temperature is reinitialized.

[♡] Henceforth, all the density plots — which we assume for the sake of argument to be normalized — will use the widely known jet color map with zero value as dark blue and unit value as dark red.

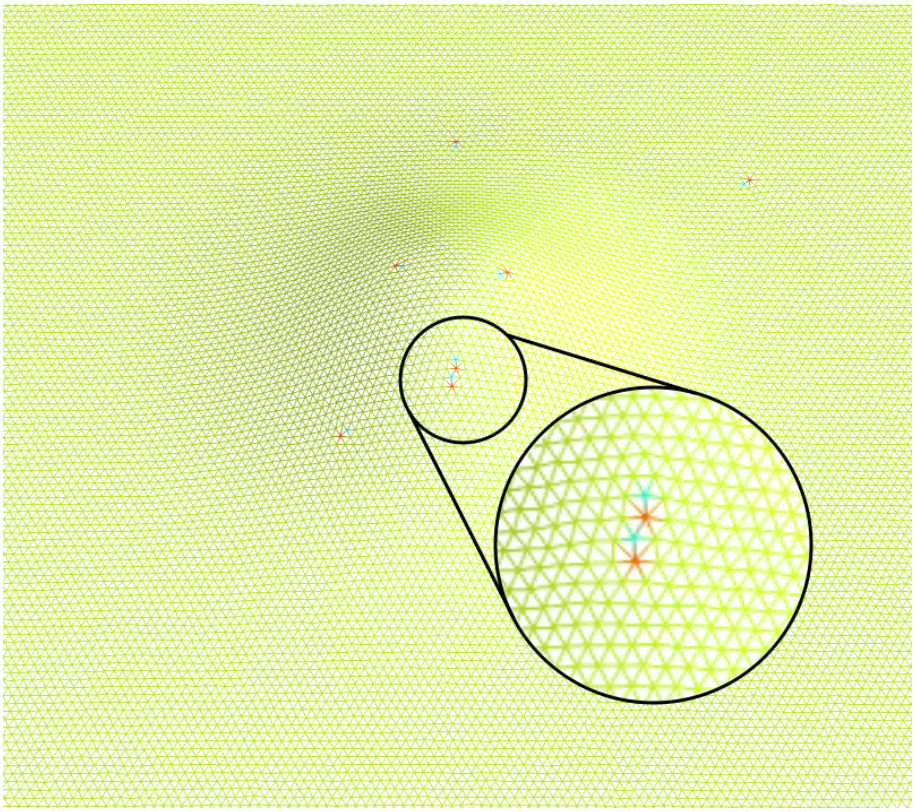

Figure 4.3: A typical end result of a simulation with $N = 17466$ particles. The triangulation is done with Delaunay triangulation. Yellow particles have six neighbors. Red particles have seven neighbors and blue particles have five neighbors. Note how dislocations are oriented with respect to the bump. This simulation is done at $\frac{A}{L} = 0.125$ and $KL = 5\sqrt{5}$, for 10000 time steps. The temperature is initialized at $T = 0.0022$ (a.u.). This image was cropped to fit this thesis.

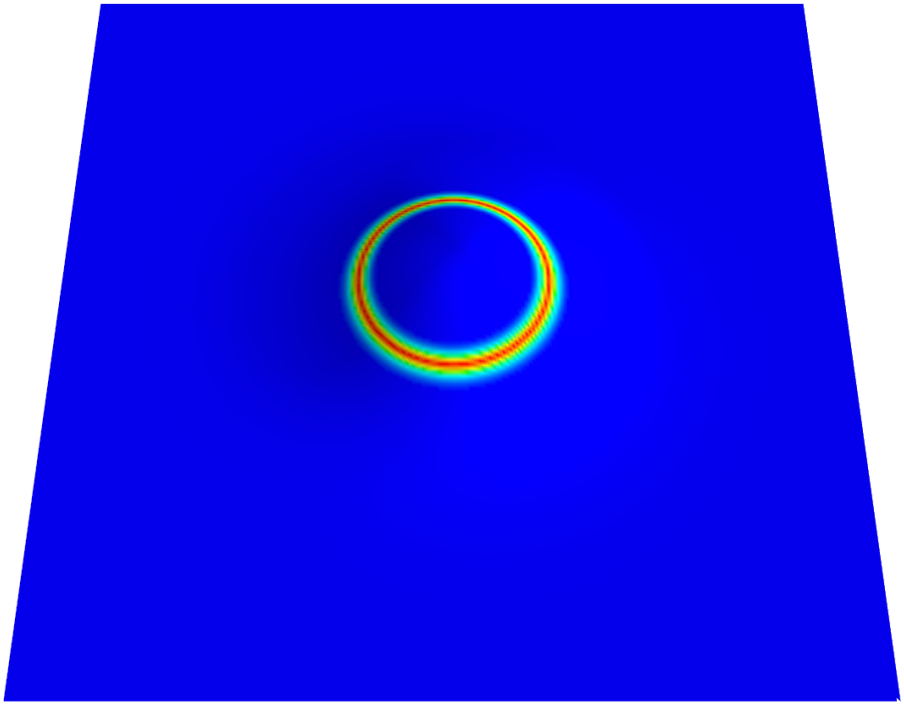

Figure 4.4: The theoretical density of dislocations according to eq. (4.48) for a Gaussian bump with $\frac{A}{L} = 0.125$ and $KL = 5\sqrt{5}$. The color map is given on page 92 footnote ♡.

and we find some discrepancies with the theoretical result plotted in fig. 4.4. Firstly, we observe a sixfold symmetry in fig. 4.5. This sixfold symmetry is due to the discrete nature of the Burgers vector as set by the lattice, which can be highlighted by distinguishing the six distinct dislocations. We color code the dislocations with the key given in fig. 4.6 on page 101 to find fig. 4.7. To account for this effect, we may modify the dislocation density eq. (4.48) to respect the discrete nature of the Burgers vector. This is done by minimizing the dislocation potential $D(x^\rho, \mathbf{b}(\theta))$ where θ is now discrete and set by the principal axes of the crystal. Doing so results in:

$$\sigma_6(x^\rho) \propto \mathrm{e}^{-\beta \min_{\mathbf{b}_n} D(x^\rho, \mathbf{b}_n)}, \tag{4.49}$$

where $\mathbf{b}_n$ are the discrete Burgers vectors. The modified dislocation density eq. (4.49) is plotted in fig. 4.8. Secondly, we observe dislocations far away from the bump which can be explained by realizing that dislocations nucleate in pairs and then glide to their equilibrium position. For one dislocation this means migrating to the point close to the theoretical energetic minimum, for its opposite pair this means migrating away from the bump to infinity. Since periodic boundary conditions are imposed, however, these dislocations have no way of reaching infinity and migrate to a point that minimizes their energy while respecting the constricted one-dimensional glide motion. This effect can be observed when we tile fig. 4.7 resulting in fig. 4.9. Finally, we observe that the peaks at the theoretical minima split. This phenomenon can be explained by dislocation–dislocation interactions and dislocation dynamics, see eq. (4.36) and section 4.4.4 respectively. Two dislocations may glide into each other and change their orientation if compatible; the reverse is also possible. For example two dislocations of opposite orientation can annihilate but can be spontaneously created. Likewise two dislocations with an orientational difference of $\frac{2\pi}{3}$ may form one dislocation with a mean angle. The latter is responsible for the peak splitting. Using the color coding as given in fig. 4.6 we observe that dislocation of e.g. cyan orientation at their equilibrium position occasionally split up in to two dislocations with green and blue orientation. This newly formed dislocation will then glide to to its new respective minimum. Since gliding motion is strictly one-dimensional these new minima are farther radially inward than the energetic minima described by the modified dislocation potential as plotted in fig. 4.8. The described mechanism is depicted in fig. 4.10.

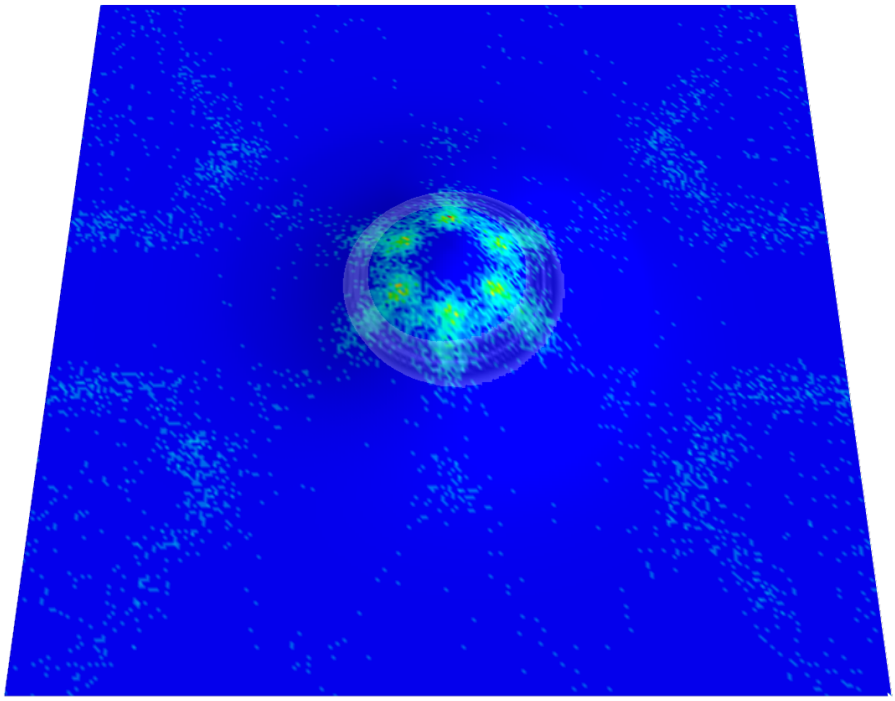

Figure 4.5: The simulated dislocation density on a Gaussian bump. The dark bands indicate the theoretically predicted minima. This plot was compiled from 1200 simulations done at $\frac{A}{L} = 0.125$ and $KL = 5\sqrt{5}$, for 10000 time steps. The temperature is initialized at $T = 0.0022$ (a.u.). The color map is given on page 92 footnote ♡.

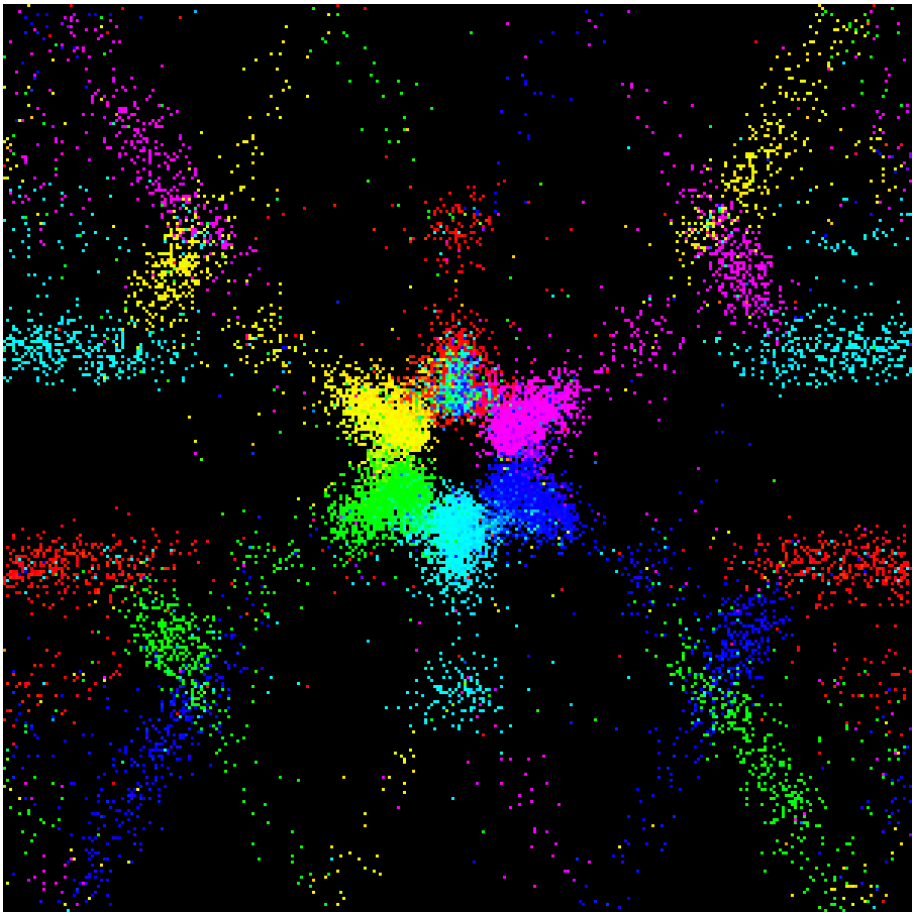

Figure 4.7: The simulated dislocation density as depicted in fig. 4.5 color coded as defined by fig. 4.6 on page 101. We observe that the color coded dislocations align as expected by energy minimization done by eq. (4.49). The occurrence of cyan in the red minimum is due to the branch cut in the $\arctan_2$ function.

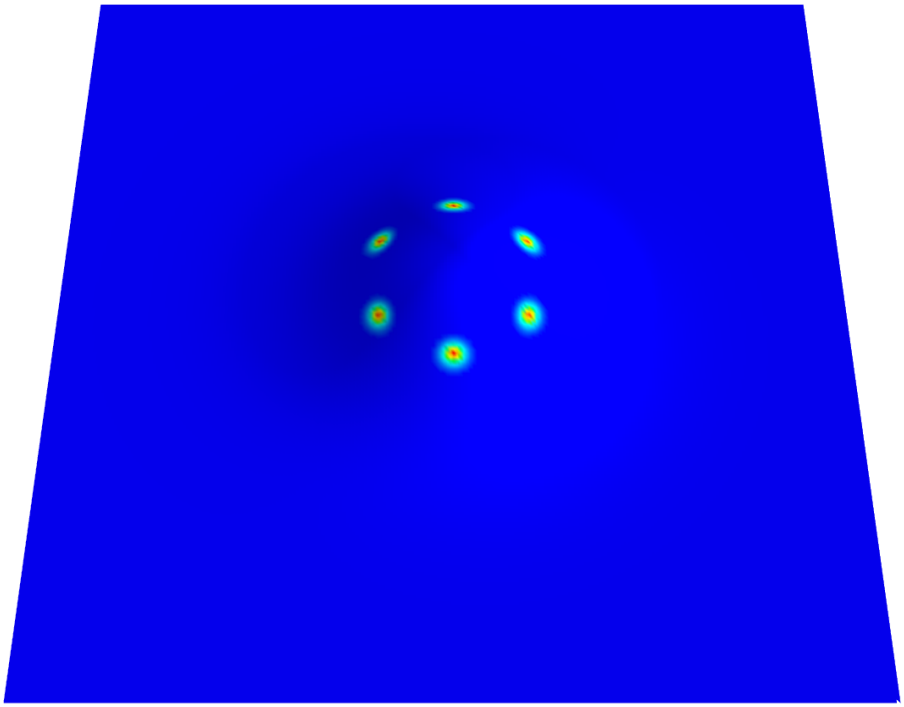

Figure 4.8: The modified theoretical density of dislocations according to eq. (4.49) for a Gaussian bump with $\frac{A}{L} = 0.125$ and $KL = 5\sqrt{5}$. The color map is given on page 92 footnote ♡.

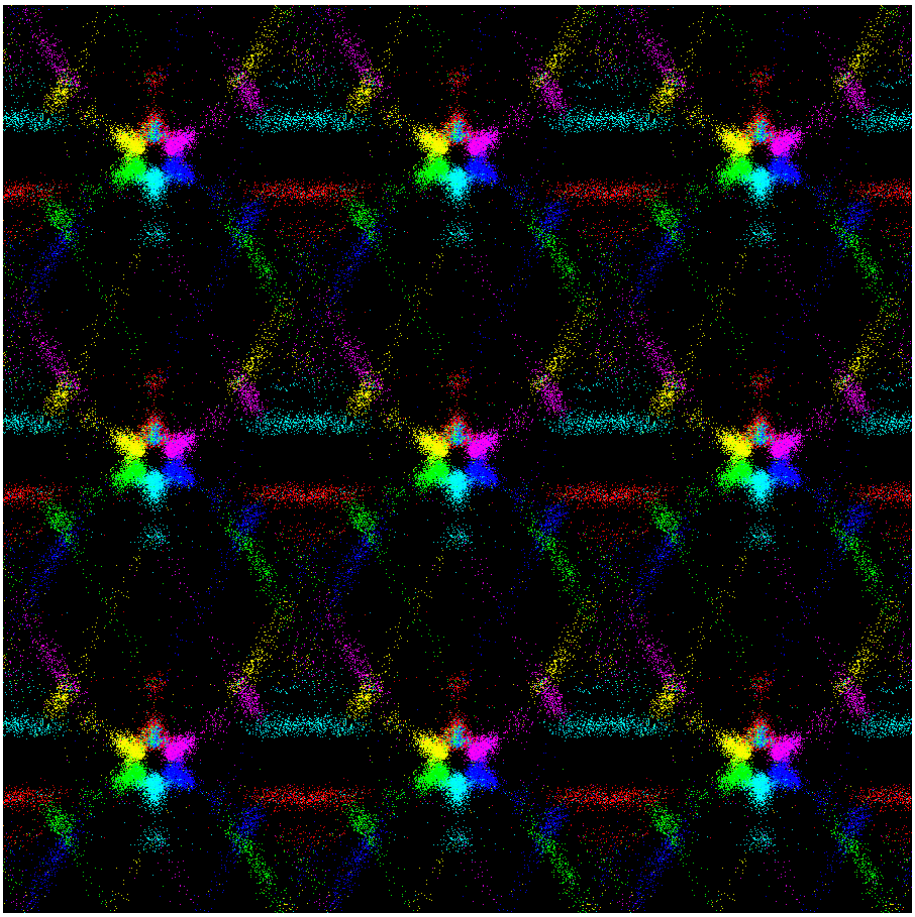

Figure 4.9: A 3×3 tiling of fig. 4.7. We observe that the color coded dislocations align as expected by energy minimization done by eq. (4.49). Additionally, we observe that an important number of dislocations do not fit in this sixfold pattern. They glide away from their nucleation point towards a lower energetic point. The red and cyan dislocation are trapped between the opposite minima, the blue, magenta, yellow and green dislocations are free to roam around (one-dimensionally) forming a long tail.

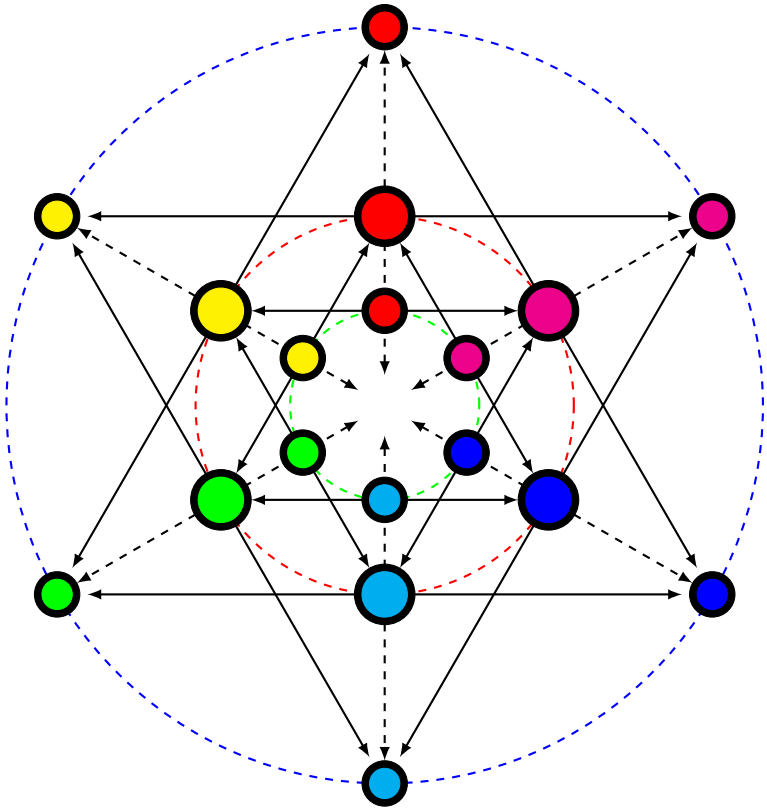

Figure 4.10: The depiction of the mechanism by which the energetic minimum is split. The large colored nodes are the predicted dislocation potential minima. The smaller and inner colored nodes are the minima by the dislocation splitting and gliding. The solid arrows are glide directions for their respective node, the dashed arrows are the climb directions. A dislocation that for instance resides at the red node and then splits into two dislocations with their Burgers vectors rotated by $\frac{\pi}{3}$ compared to the initial dislocation will glide towards their new inner minima. The dislocation cannot climb because this requires diffusive mechanisms, and is therefore stuck in its new minimum.

A similar analysis can be conducted on the egg carton surface, see eq. (4.40). Theoretically, the dislocation density for the egg carton surface is plotted fig. 4.11. The dislocation density of the simulations are found in fig. 4.12. As this structure is periodic, the periodic boundary conditions interfere less with the dislocation distribution. The theoretical dislocation density does not account, however, for dislocation–dislocation interactions, which is likely the reason why the minima in the simulations differ a little from the theoretical estimate.

4.4.8 Conclusions and outlook

It is hard to draw any firm conclusions. It seems, however, that for low temperatures, the simulations theoretical estimates and numerical experiment are in qualitative agreement, although more investigation is required. A thorough test would be to compare the results of the dynamics to a Monte Carlo simulation. Such Monte Carlo simulations would simulate dislocation dynamics in the presence of curvature similar to Pafka et al. [140] and Saito [165] using the Hamiltonian stated in eq. (4.37) — without neglecting the dislocation–dislocation potential eq. (4.36). If the Monte Carlo simulations match the molecular dynamics simulations we will understand the behavior of multiple dislocations in the presence of curvature. The results might differ because curvature influences the dislocation–dislocation interaction. One could measure the dislocation–dislocation interaction from the simulations and plug them back into the Monte Carlo, see also Crocker et al. [150].♠

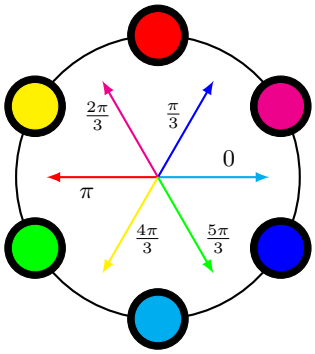

Figure 4.6: The arrows color coding the six distinct orientations of the Burgers vectors as imposed by the six principle lattice directions. The colored circles schematically indicate the spatial positions of distinct minima per orientation of the Burgers as found by eq. (4.49).

♠See the forthcoming doctorate thesis of C. van der Wel (Leiden University) for a generalization of Crocker et al. [150] in the presence of curvature.

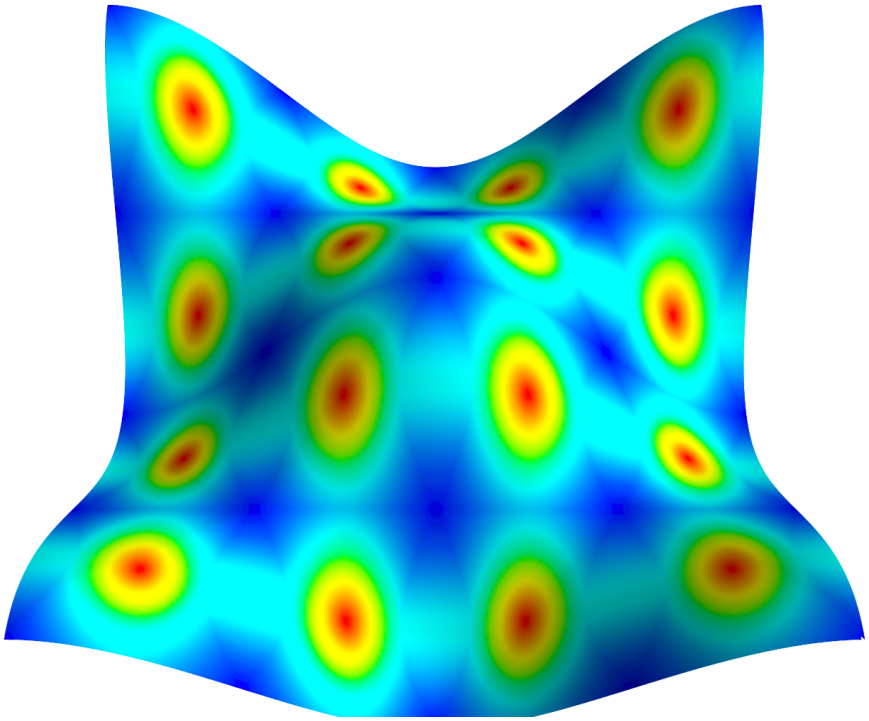

Figure 4.11: The theoretical density of dislocations according to eq. (4.38) for a egg carton surface with $K_x L = K_y L = 2\pi$. The color map is given on page 92 footnote ♡.

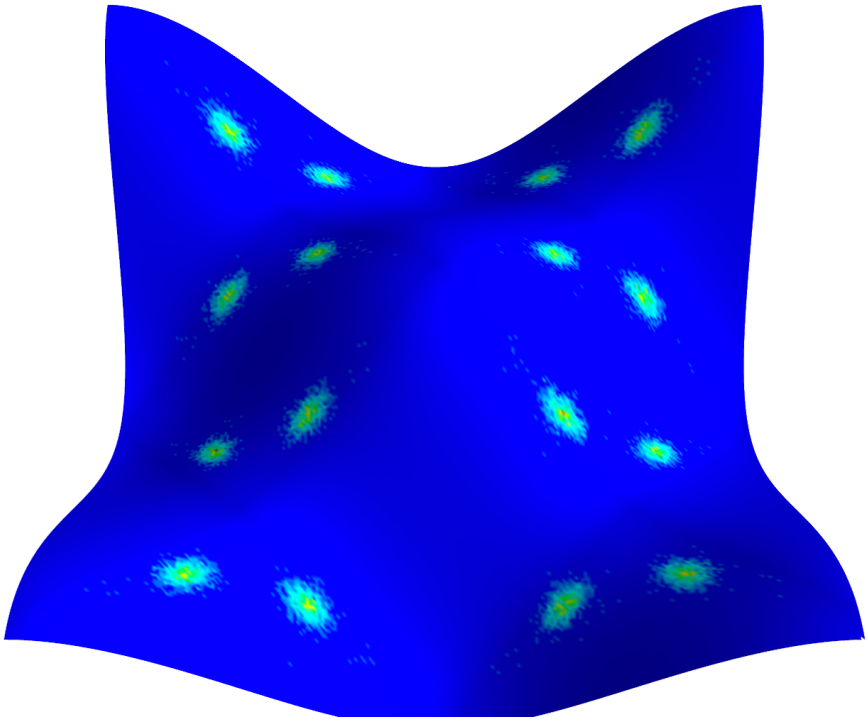

Figure 4.12: The simulated dislocation density on a egg carton surface. This plot was compiled from 1200 simulations done at $\frac{A}{L} = 0.1$ and $K_x L = K_y L = 2\pi$, for 10000 time steps. The temperature is initialized at $T = 0.001$ (a.u.). The color map is given on page 92 footnote ♡.